Supporting Information

Synthesis of Nanosized Metal Sulfides Using Element Sulfur in Formamide: Implications for Energy conversion and Optical scenarios

Kai Sun, Shuchang Song, Anuj Kumar, Zhicheng Shang, Xinxuan Duan, Shiyuan Wang, Shubo Tian, Jialun Tang, Daojin Zhou*, Xiaoming Sun*

[a]. State Key Laboratory of Chemical Resource Engineering, Beijing Advanced Innovation Center for Soft Matter Science and Engineering, Beijing University of Chemical Technology, Beijing 100029, China.

[b]. Department of Chemistry, Institute of Humanities and Applied Science, GLA University, Mathura 281406, India.

Daojin Zhou: zhoudj@mail.buct.edu.cn

Jialun Tang: tangjialun90@163.com

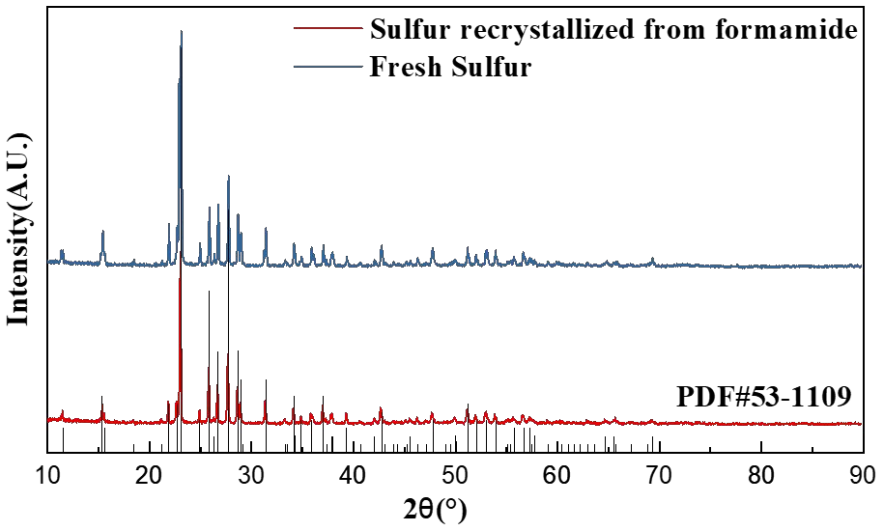

Figure S1. XRD patterns of fresh sulfur and recrystallized sulfur.

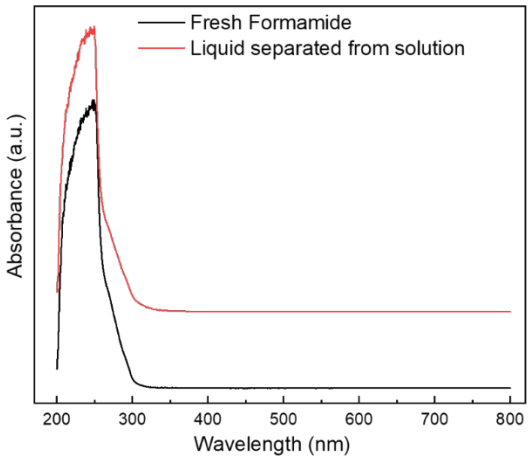

Figure S2. UV-visible spectra of separated formamide and fresh formamide

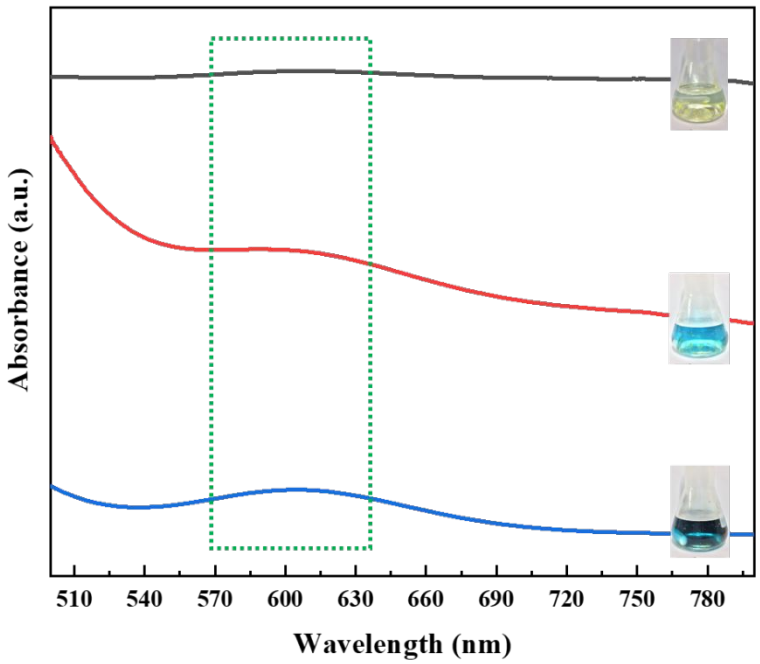

Figure S3. Ex-situ UV spectrums of sulfur-FA solution at different stages.

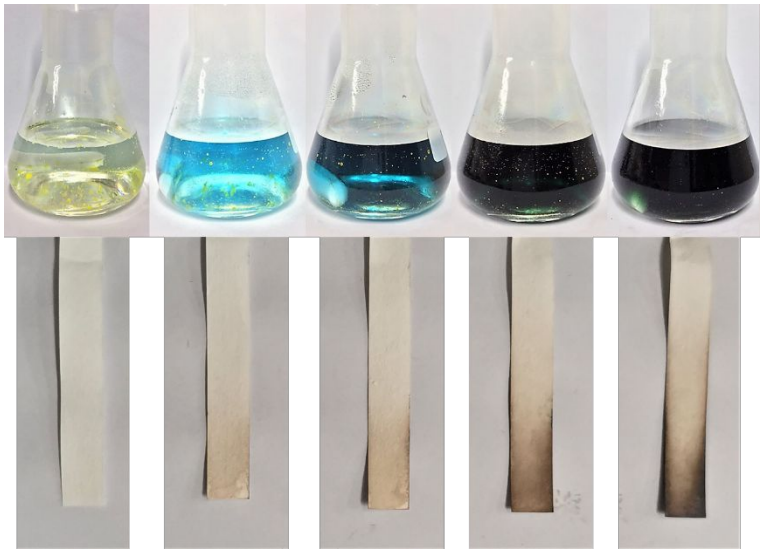

Figure S4. Digital images of the color change of sulfur over time in FA at 160℃ in 3 minutes intervals and the corresponding pictures of Lead Acetate Test Paper.

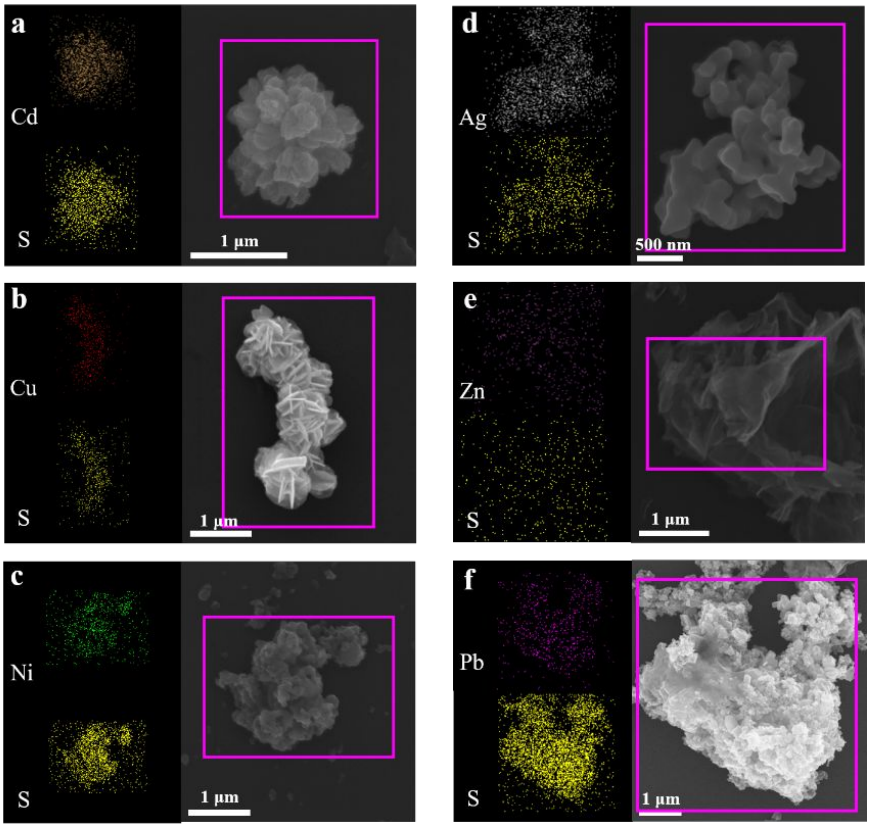

Figure S5. SEM images and SEM-element mappings of the as-prepared (a) CdS, (b) CuS, (c) NiS_2, (d) Ag_2S, (e) ZnS and (f) PbS.

Table S1 Calculation process of D values.

(h k l)	2θ/ °	FWHM/ °	D/ nm
(100)	24.7906	0.61247	13.13849
(002)	26.4990	0.49170	16.42107
(101)	28.1359	0.73585	11.01070
(102)	36.5961	1.68733	4.90576
(110)	43.6715	0.72592	11.66285
(103)	47.8198	1.27825	6.72517
(112)	51.8451	1.09377	7.98867

In order to avoid the size inaccuracy caused by the region selection during electron microscope observation, we calculated the particle size from the XRD data of the basically spherical CdS crystal. We have selected 7 crystal planes with stronger signals in small angles (2θ< 60°). They are: (100), (002), (101), (102), (110), (103), (112), K=0.89, and λ=0.15405 nm. The calculated the D values according to the Scherer equation are about 13.1 nm, 16.4 nm, 11.0 nm, 4.9 nm, 11.7 nm, 6.7 nm, 8.0 nm, and the average size of a single unit cell is 10.3 nm. Compared with the data obtained by observation under the electron microscope (about 40 nm), the two data are both correct considering the influence of agglomeration. The calculation process is shown in the following Table S1.

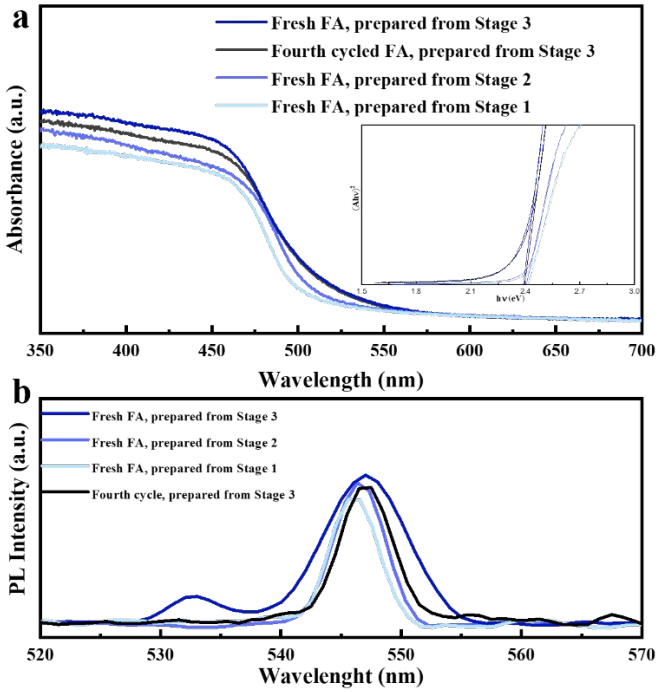

Figure S6. (a) and (b) are Photoluminescence (PL) spectra of as prepared CdS nanoparticles.

The optical properties of CdS nanoparticles are studied. The as prepared CdS with fresh FA and fourth cycled FA shared an almost same band gap value (2.39 and 2.40, as shown in the inset of Figure RS5 a). The relationship between the crystal size and its optical properties has been studied[1] (New J. Chem. 2015, 39 (12), 9442–9453.), which illustrates that size is the key factor affecting the single crystal phase CdS fluorescence emission wavelength. Since the as synthesized CdS are basically share the same size distribution, the peak positions of their PL spectrums are basically close, the emission maxima band position is ~547 nm.

Table S2. Comparison of main experimental parameters used in some major traditional preparation methods and the FA based method of this work.

Samples	**Preparation strategy**	**Precursors**	**Temperature and time of Sulfurization reaction**	**Main ingredients**	**References**
CdS	solvothermal reaction	no precursor	160℃, 24h	oilamine, thioaceylamide, cadmium acetate	2
CdS	thermal decomposition	cadmium thiourea complexes	300℃, 3h	thiourea, cadmium salts	1
$NiFeS_2$	hydrothermal reaction	no precursor	180℃, 4h	oilamine, thioaceylamid, ethanol, nickel salt and iron salt	3
$NiFeS_2$	chemical vapor deposition	nickel iron hydroxide	400℃, 1h	ammonium fluoride, urea, sulfur powder, nickel salt and iron salt	4
PbS, ZnS, CdS, MnS,	co-precipitation	no precursor	220℃, 1h for PbS; 320℃, 1h for ZnS; 140℃, 20h for CdS;	oilamine, sulfur powder, metal salt	5

			240℃, 2h for MnS		
Ni_3S_4 $Cu_{1.8}S$	co-precipitation	no precursor	220℃, 1h for Ni_3S_4; 182℃, 1 h for $Cu_{1.8}S$	oleylamine, trioctylphosphine, sulfur powder, o-dichlorobenzene, cadmium acetate	6
CdS	solvothermal reaction	MoO_3	200℃, 24h	thioaceylamide, cadmium acetate	7
CuS	solvothermal reaction	no precursor	150℃, 24h	ethylene glycol, sulfur powder, copper nitrate, CTAB	8
NiS_2, $NiFeS_2$	mechanical alloying	no precursor	25℃, 4h for NiS_2; 25℃, 4.5h for $NiFeS_2$	metal and sulfur powders	9
CdS, ZnS, CuS, NiS_2, PbS, Ag_2S	co-precipitation	no precursor	160℃, 10min	formamide, sulfur powder, metal salt	this work

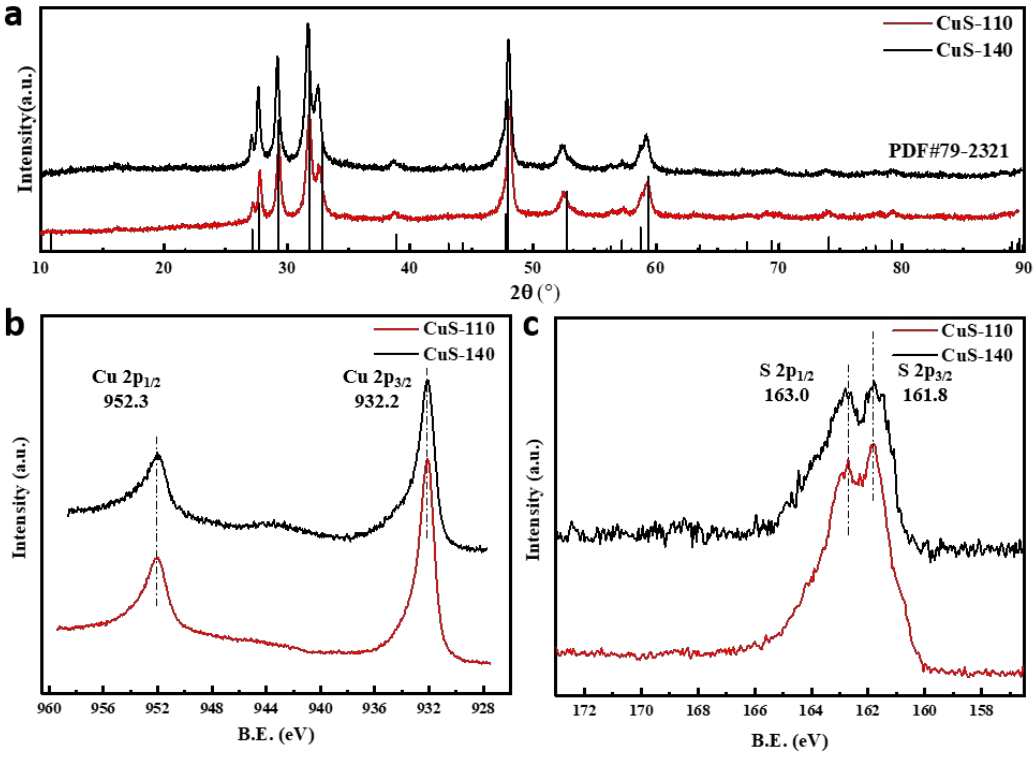

Figure S7. (a) XRD patterns of as prepared CuS. XPS data of as prepared CuS: (b) Cu 2p, (c) S 2p.

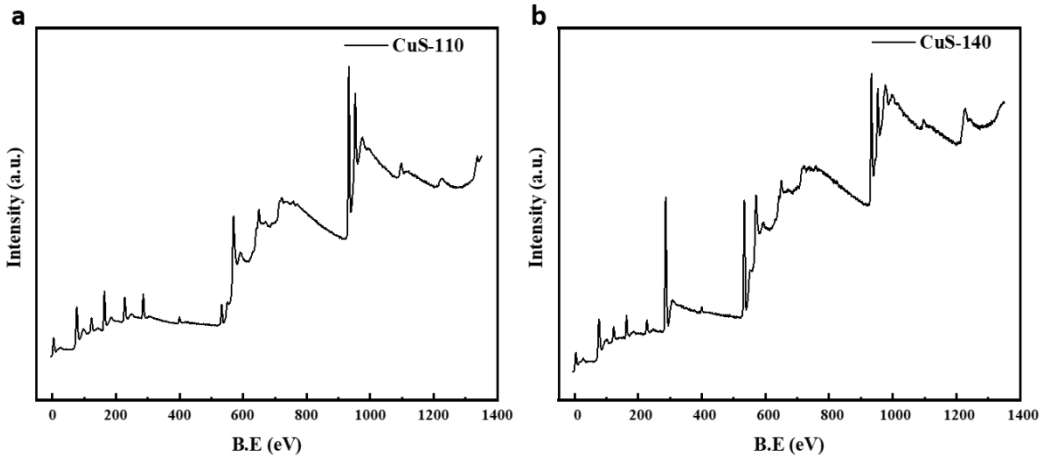

Figure S8. XPS data of as prepared CuS: (a) survey of CuS-110, (b) survey of CuS-140.

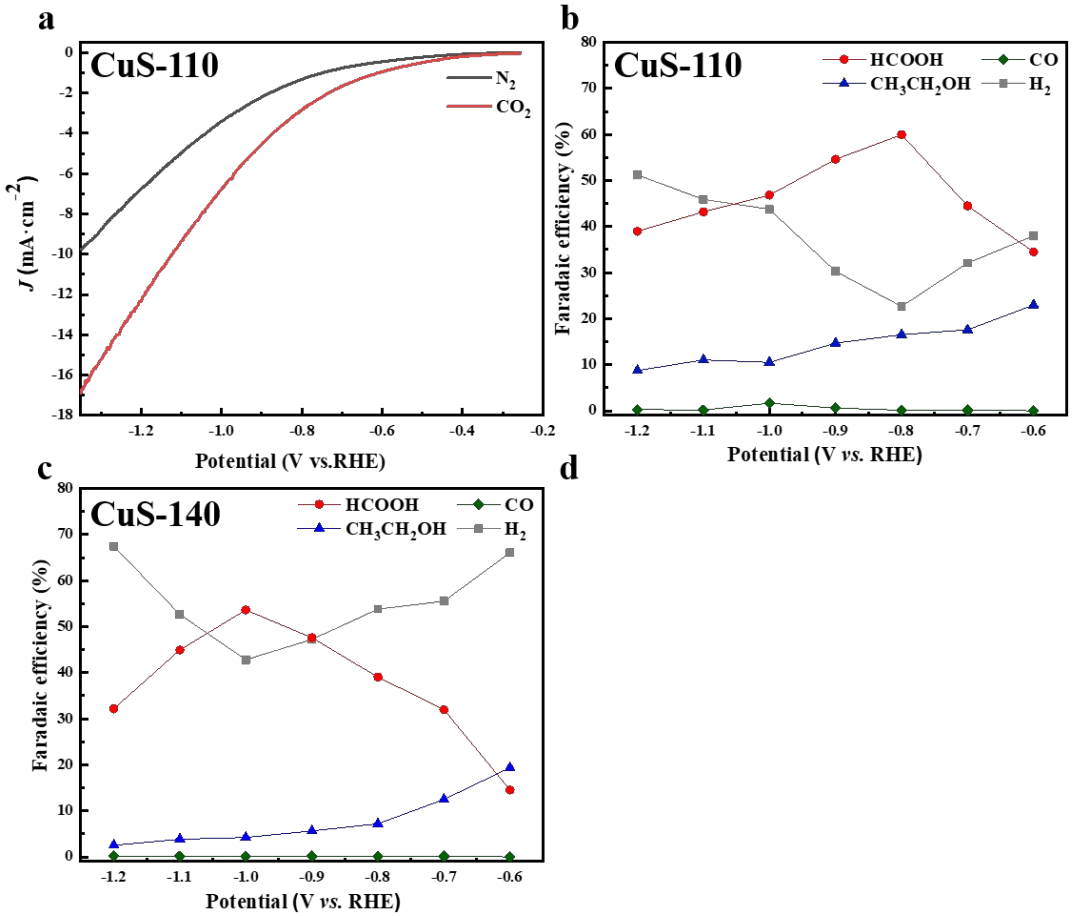

Figure S9. CO_2 electroreduction performance. (a) LSV curves in N_2-and CO_2-saturated solutions; faradaic efficiencies for HCOOH, CH_3CH_2OH, CO and H_2 at various applied potentials of (b) CuS-110 and (c) CuS-140.

Each CO_2 electroreduction experiment is performed in an electrochemical cell consisting of a working and a counter electrode compartment, separated by a Nafion-117 proton exchange membrane to prevent the oxidation of CO_2 reduction products. To identify the reduction products, gas chromatography (GC) and ^1H nuclear magnetic resonance (NMR) analysis is carried out to quantify the gas and liquid products, respectively. In the N_2-saturated solution (Figure S9 a), the increase in the current after -0.5 V is ascribed to the hydrogen evolution, which competes with the CO_2 reduction reaction[10,11]. Meanwhile, the CuS-110 illustrates a clearly increased reduction current in the CO_2-saturated electrolyte, which clearly suggesting that the reduction of

CO_2 is catalytically more favourable with respect to the HER. The faradaic efficiencies of the electrocatalytic CO_2 reduction products as a function of the applied potential are reported in Figure S9 b and c. CuS-110 has a worth-noticing capability of producing HCOOH, which exhibits a maximum faradaic efficiency (FE) of 62% at -0.8 V. The CH_3CH_2OH production displays a maximum FE of 24% at -0.6V. The total faraday efficiency of HCOOH and CH_3CH_2OH is close to 80%. Additionally, we find that the FE for H_2 production steadily decreased as the amount of carbonaceous products increased before -0.8V. For comparison, the CO_2 electroreduction activity of sample CuS-140 has been characterized. This sample containing CuS nanoparticles instead of nanosheets shows a maximum FE of 55% for HCOOH production (Figure S9 c) at -1.0V, which is smaller than that of CuS-110, at the same time, the H_2 production is much higher than that of CuS-110. This comparison demonstrates that the nanosheet morphology is more favourable for mass transport and active site exposure and thereby improves the CO_2 electroreduction performances, consistent with the previously reported result for SnO_2 nanosheets[12,13]

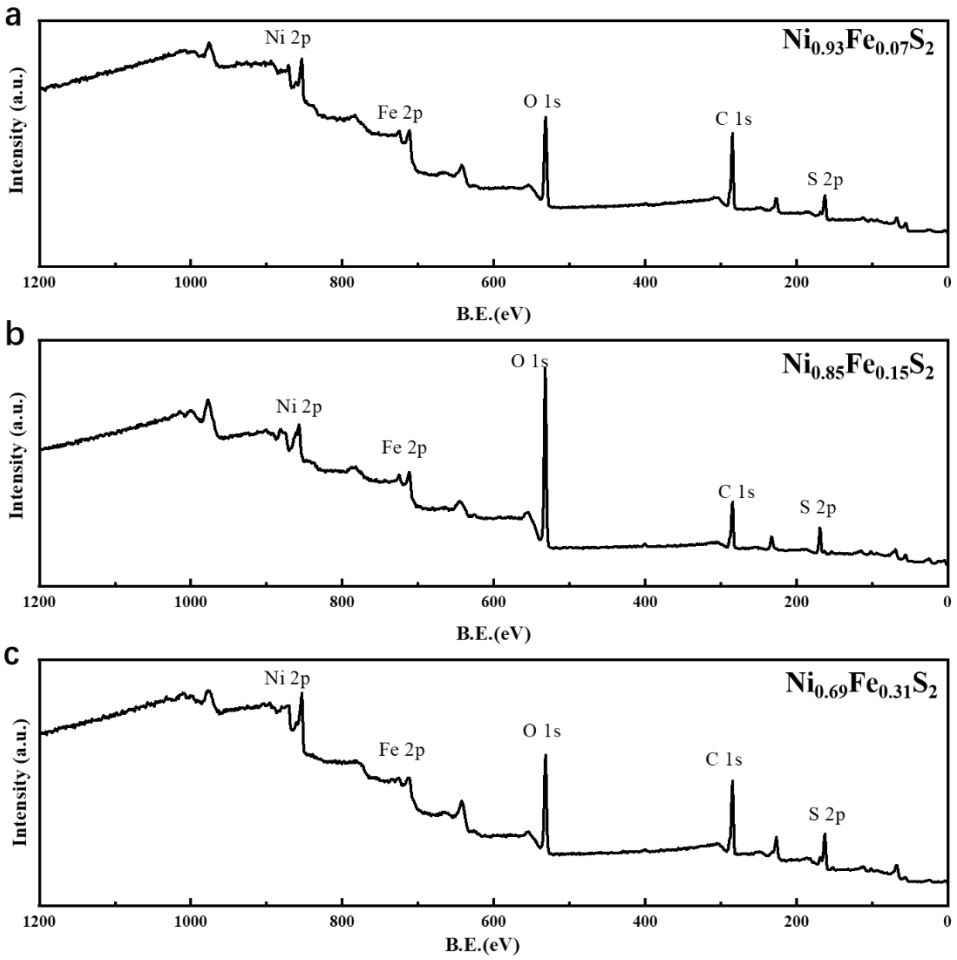

Figure S10. XPS data of as prepared $Ni_xFe_{1-x}S_2$ samples: (a) $Ni_{0.93}Fe_{0.07}S_2$, (b) $Ni_{0.85}Fe_{0.15}S_2$, (c) $Ni_{0.69}Fe_{0.31}S_2$.

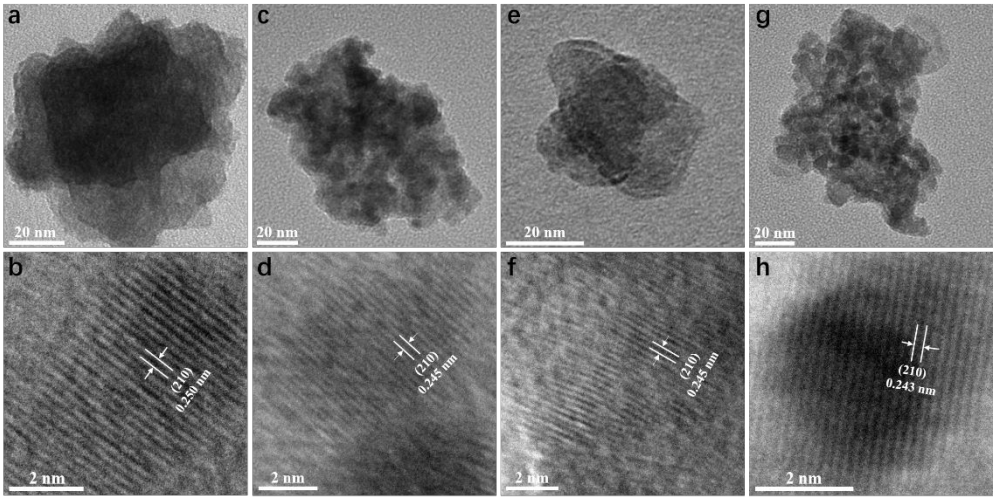

Figure S11. TEM and HRTEM images of as prepared: (a, b) NiS_2, (c, d) $Ni_{0.93}Fe_{0.07}S_2$, (e, f) $Ni_{0.85}Fe_{0.15}S_2$, (g, h) $Ni_{0.69}Fe_{0.31}S_2$.

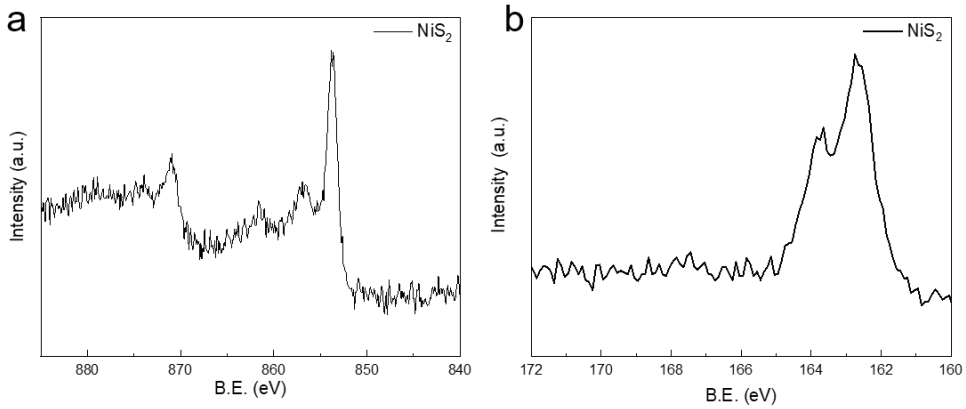

Figure S12. XPS data of as prepared NiS_2: (a) Ni 2p, (b) S 2p.

The XPS spectrum of Ni 2p (Figure S12 a) and S 2p (Figure S12 b) from pure NiS2 synthesized under the same conditions. The peak located at 853.6 eV and 162.7 eV are correspond to Ni 2p3/2 and S 2p3/2(J. Solid State Chem. 33, 17 (1980)).

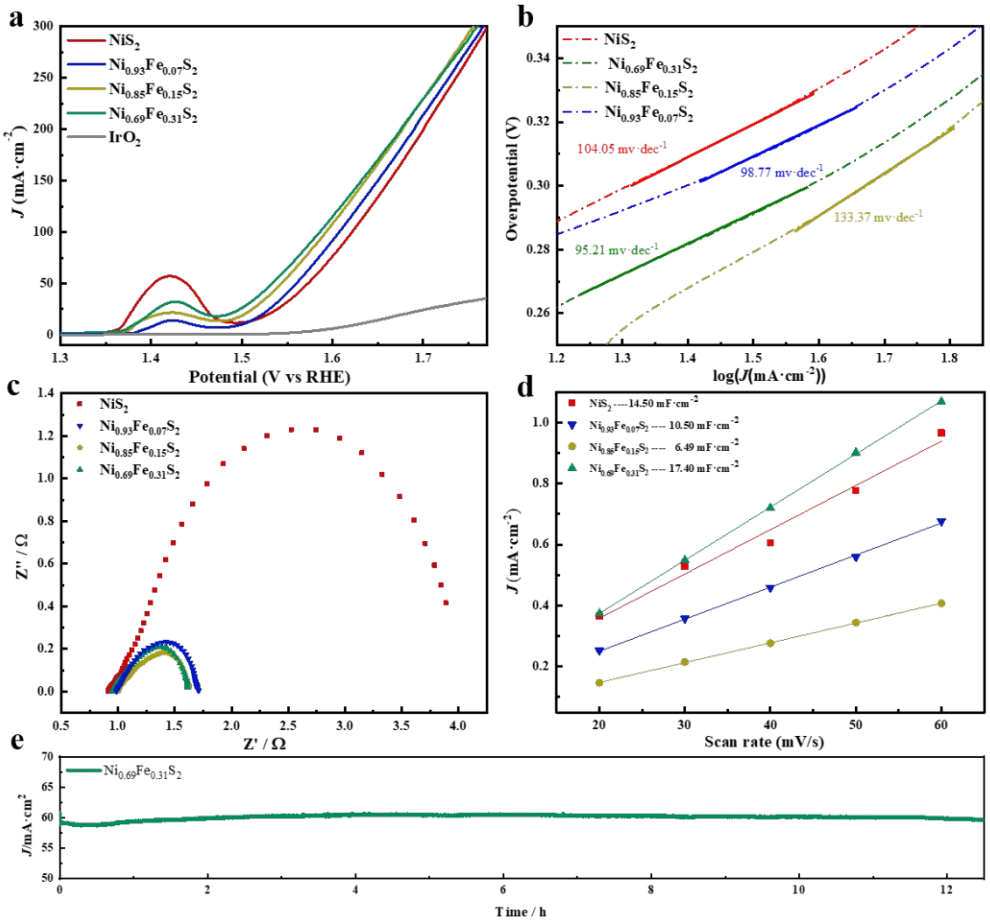

Figure S13. OER activity of as prepared $Ni_xFe_{1-x}S_2$ samples and IrO_2: (a) polarization curves, (b) Tafel plots, (c) Nyquist plots, (d) double-layer capacitances, and (e) stability test of $Ni_{0.69}Fe_{0.31}S_2$ through chronoamperometry for more than 12 h in 1.0 M KOH.

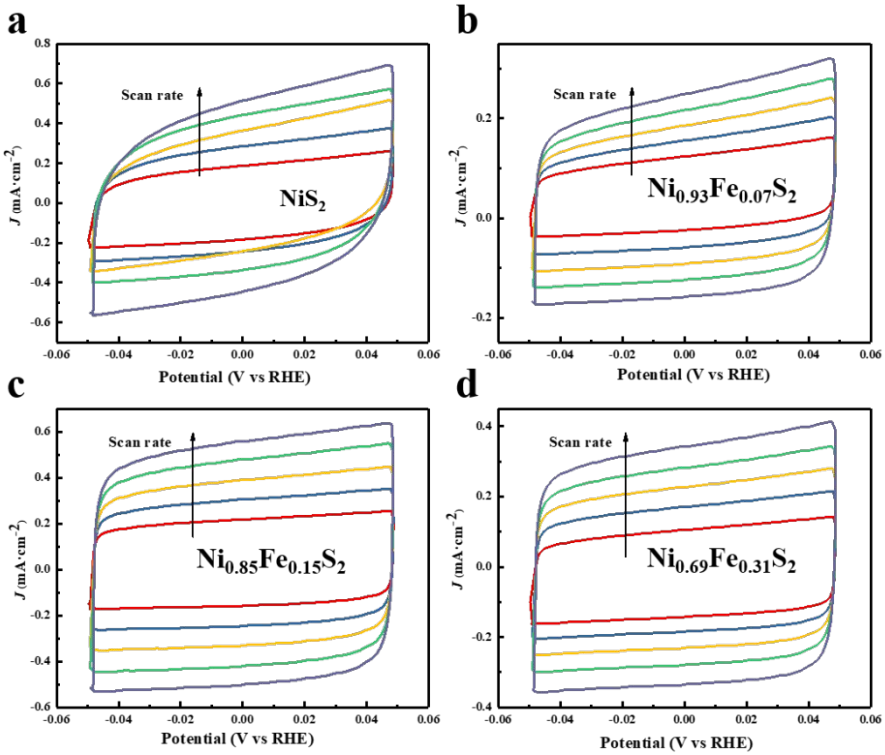

Figure S14. Cyclic voltammogram (CV) of double-layer capacitance (C_{dl}) measurement of (a) NiS_2, (b) $Ni_{0.93}Fe_{0.07}S_2$, (c) $Ni_{0.85}Fe_{0.15}S_2$, (d) $Ni_{0.69}Fe_{0.31}S_2$.

Table S2. The electrochemically active surface area (ECSA) and roughness factor (RF) of all samples.

Sample	Cdl (mF)	Cs (mF·cm^{-2})	ECSA (cm^2)	GSA (cm^2)	RF
NiS_2	29.00	0.04	725.0	2.00	362.5
$Ni_{0.93}Fe_{0.07}S_2$	12.98	0.04	324.5	2.00	162.25
$Ni_{0.85}Fe_{0.15}S_2$	21.00	0.04	525.0	2.00	262.5
$Ni_{0.69}Fe_{0.31}S_2$	34.80	0.04	870.0	2.00	435

The OER performances of $Ni_xFe_{1-x}S_2$ samples were recorded in 1.0 M KOH solution. The LSV polarization curves of all samples were shown in Figure S13 a. The NiS_2 showed a better OER activity but still require a overpotential of 342 mV at 50 mA·cm^{-2}. However, when Fe was doped in to NiS_2, the binary metal sulfides ($Ni_xFe_{1-x}S_2$) showed considerable OER activity improvement as compared toNiS_2. The best performance was achieved by $Ni_{0.69}Fe_{0.31}S_2$ and the overpotential of which was 300 mV at 50 mA·cm^{-2} followed by 312 mV of $Ni_{0.85}Fe_{0.15}S_2$ and 328 mV of $Ni_{0.93}Fe_{0.07}S_2$. Thus, the incorporation of Fe in NiS_2 leads to enhanced OER activity. Furthermore, to estimate the OER kinetics of as-prepared samples in alkaline, the Tafel plots and Nyquist plots were carried out and showed in Figure S13 b and c respectively. The Tafel slope of $Ni_{0.69}Fe_{0.31}S_2$ is 98.77 mV·dec^{-1}, which is smaller than that of $Ni_{0.85}Fe_{0.15}S_2$ (133.37 mV·dec^{-1}), $Ni_{0.93}Fe_{0.07}S_2$ (98.77 mV·dec^{-1}) and NiS_2 (104.05 mV·dec^{-1}). suggesting a more favorable OER reaction kinetic of $Ni_{0.69}Fe_{0.31}S_2$. This study confirmed the improved OER reaction kinetics of $Ni_{0.69}Fe_{0.31}S_2$. The Figure S13 c is utilized to fit the charge transfer impendence of all samples during OER process, in which the ohmic resistance of each sample exactly matched with their performance ($Ni_{0.69}Fe_{0.31}S_2$ (1.60 Ω), $Ni_{0.85}Fe_{0.15}S_2$ (1.64 Ω), $Ni_{0.93}Fe_{0.07}S_2$ (1.75 Ω) and NiS_2 (4.12 Ω)). Moreover, the effective surface areas of the as-prepared samples have been estimated by electrochemical active surface area (ECSA), which is positively related to double-layer capacitance (C_{dl}) derived from CV results shown in Figure S14. The Figure S13 d showed that $Ni_{0.69}Fe_{0.31}S_2$ exhibited the largest areal capacitance of 17.4 mF·cm^{-2} compared with NiS_2 (14.5 mF·cm^{-2}), $Ni_{0.93}Fe_{0.07}S_2$ (10.5 mF·cm^{-2}) and $Ni_{0.85}Fe_{0.15}S_2$ (6.5 mF·cm^{-2}). The calculated ECSA values for all samples are illustrated in Table S2. The results confirmed that the $Ni_{0.69}Fe_{0.31}S_2$ possesses the largest active surface area among all electrocatalysts. The large electrochemically active area of $Ni_{0.69}Fe_{0.31}S_2$ may be attributed to the presence of abundant active sites for OER, which is caused by the increase of Fe^{3+}. Stability is another important criterion for judging an efficient electrochemical OER catalyst. As shown in Figure S13 e, a long-time current density (*i*-t) curve for OER was conducted on $Ni_{0.69}Fe_{0.31}S_2$ through chronoamperometry in 1.0 M KOH. The *i*-t curve shows negligible loss in the current density after 12 hours, which clearly indicates the excellent electrostability. The calculation of ECSA and RF can be based on the following equations:

$$ECSA = \frac{C_{dl}}{C_s}$$

$$RF = \frac{ECSA}{GSA}$$

where C_{dl} is measured double layer capacitance of samples in 1.0 M KOH (mF), C_s represents the specific capacitance of electrocatalysts (C_s = 0.04 mF·cm^{-2} in 1.0 M KOH) and GSA is the geometric surface area of the as-prepared samples (2.00 cm^2).

Experimental Methods

Single Metal sulfide synthesis

5 millimole of elemental sulfur (cyclo-S_8) was added into a conical flask containing 30 ml formamide. The obtained mixture was stirred at 160 ℃ for 10 minutes, a blue transparent solution (at this point, the solution is denoted by "A") was observed. In behind, Metal nitrate mixed in another conical flask containing 30 ml formamide, stirred at 110 ℃ for 3 minutes to preheat and the obtained solution was denoted by "B". Then, solution "A" was poured into solution "B" rapidly, as shown in the figure 1, a gentle stirring was continued for another 10 minutes at 110 ℃, after which a uniform suspension was prepared. After centrifugation and washing with CS_2 to remove the residual sulfur element on the sample surface, a powder product was collected after drying in at 60℃ for 1 hour.

Fe doped NiS_2 synthesis

5 millimole of elemental sulfur (cyclo-S_8) was added into a conical flask containing 30 ml formamide. The obtained mixture was stirred at 160 ℃ for 10 minutes, a blue transparent solution (at this point, the solution is denoted by "A") was observed. In behind, $Fe(NO_3)_3 \cdot 9H_2O$ and $Ni(NO_3)_2 \cdot 6H_2O$ totaling 5 millimole was mixed at a ratio of Ni:Fe=9:1, 8:2, 6:4 in another conical flask containing 30 ml formamide, stirred at 110 ℃ for 3 minutes to preheat and the obtained solution was denoted by "B". Then, solution "A" was poured into solution "B" rapidly, as shown in the figure 1, a gentle stirring was continued for another 10 minutes at 110 ℃, after which a uniform suspension was prepared. After centrifugation and washing with CS_2 to remove the residual sulfur element on the sample surface, a powder product was collected after drying in at 60℃ for 1 hour.

CdS synthesis with reused FA

50 millimole of elemental sulfur (cyclo-S_8) was added into an Erlenmeyer flask containing 100 ml formamide. The obtained mixture was stirred at 160 ℃ for 15 minutes to obtain a blue transparent solution (denoted as A). 5 millimole of $Cd(NO_3)_2 \cdot 4H_2O$ was mixed in another conical flask containing 100 ml formamide, stirred at 110 ℃ for 5 minutes to preheat and the obtained colourless transparent solution was denoted by "B". Then, solution "A" was poured into solution "B" rapidly, a gentle stirring was continued for another 10 minutes at 110 ℃ to obtain a uniform suspension. After the suspension was cooled to room temperature, a yellow cadmium sulfide powder and a supernatant liquid were obtained by centrifugation (10000 rpm, 15mins). The supernatant liquid was replenished to 200 ml with fresh formamide, divided into two on average, and the same operation was performed for a total of four times.

Characterization of samples

The morphologies of synthesized crystalline products were characterized by field-emission scanning electron microscope (SEM; JEOL JSM6335, 20 kV) with an energy dispersive X-ray spectroscopy (EDS) system, and transmission electron microscopy (TEM; FEI Tecnai G^2 20), and high-resolution TEM (HRTEM) (JEOL JEM-2100). The XRD patterns were collected on Shimadzu XRD-6000 with Cu Kα radiation (40 kV, 30 mA, λ = 1.5418 Å), at a scan rate of 5(°) min^{-1}, recorded

with 2θ ranging from 10° to 90°. The XPS measurements were carried out with a PHI Quantera II XPS Scanning Microprobe. For H_2S test, 20μL of the corresponding solution was dropped on the wet lead acetate test paper and wait for it to dry.

Electrochemical measurements

The electrocatalytic OER performance of the prepared materials were performed in 1M KOH (aq.) solution by employing a three-electrode system on an electrochemical workstation (CHI660D, Chenhua, Shanghai). The saturated calomel electrode (SCE) and platinum electrode were used as the reference and the counter electrode, respectively. The working electrode was prepared by using catalyst ink and Ni foam. The Ni foam (1 × 1 cm^2) was used as catalyst support. For the preparation of working electrode, 2 mg of sample powder and 20 μL of Nafion were dispersed in 0.5 mL ethanol, keep ultrasonication for 1 h to form a homogeneous catalyst ink. The prepared ink was loaded onto Ni foam (1 × 1 cm^2) using a micropipette to achieve a mass loading of 2 $mg \cdot cm^{-2}$. The same method was applied for the preparation of other working electrodes of the synthesized metal sulfides. After 20 cyclic voltammetric (CV) scans, the linear sweep voltammetric (LSV) polarization data were collected at a scan rate of 5 $mV \cdot s^{-1}$ to minimize capacitive current. AC impedance measurements were carried out in the same configuration at open-circuit voltage from 0.1 to 10^5 Hz with an AC voltage of 5 mV. The stability of the electrode was measured by applying a constant potential to achieve an initial current density of 50 $mA \cdot cm^{-2}$ for 12 h. The ECSA was determined by measuring the capacitive current associated with double-layer charging from the scan-rate dependence of CVs. The potential window and scan rates were used as -0.05–0.05 V (vs RHE, 1 M KOH) and 20-60 $mV \cdot s^{-1}$ respectively. The double-layer capacitance (Cdl) was estimated by obtaining the slope from the plotting of current density at 0 V (vs SCE, 1 M KOH) against the scan rate.

The electrochemical measurements of CO_2RR were carried out using an electrochemistry workstation (CHI 660e, CH, Shanghai.). A homemade gas-tight H-type electrochemical cell separated by a cation exchange membrane (Nafion N117, DuPont) was used. The electrolyte was 0.1 M $KHCO_3$ aqueous solution. The carbon paper (1 × 1 cm^2) was used as catalyst support. For the preparation of CuS working electrode, 2 mg of CuS powder and 20 μL of Nafion were dispersed in 0.5 mL ethanol, keep ultrasonication for 1 h to form a homogeneous catalyst ink. The prepared CuS ink was loaded onto carbon paper (1 × 1 cm^2) using a micropipette to achieve a mass loading of 2 $mg \cdot cm^{-2}$. A graphite rod was used as the counter electrode and an Ag/AgCl electrode was used as the reference electrode. The reference electrode was periodically calibrated. For the electrochemical measurements, the CO_2 with flow rate of 20 sccm was delivered into the cathodic compartment (directly connected to the gas chromatograph (GC Agilent 7890B)) and was allowed to purge for 20 min prior to the beginning of experiments. Liquid products were analyzed by ^1H NMR on Agilent 600MHz DirectDrive2 spectrometers. The faradaic efficiency (FE) for the products was calculated as follows:

$$FE = \frac{eFn}{Q}$$

References

(1) Gaur, R.; Jeevanandam, P. Effect of Anions on the Morphology of CdS Nanoparticles Prepared via Thermal Decomposition of Different Cadmium Thiourea Complexes in a Solvent and in the Solid State. *New J. Chem.* **2015**, *39* (12), 9442–9453. https://doi.org/10.1039/c5nj01605c.

(2) Zhang, G.; He, P.; Ma, X.; Kuang, Y.; Liu, J.; Sun, X. Understanding the "Tailoring Synthesis" of CdS Nanorods by O_2. *Inorg. Chem.* **2012**, *51* (3), 1302–1308. https://doi.org/10.1021/ic201119c.

(3) Ni, B.; He, T.; Wang, J. O.; Zhang, S.; Ouyang, C.; Long, Y.; Zhuang, J.; Wang, X. The Formation of $(NiFe)S_2$ Pyrite Mesocrystals as Efficient Pre-Catalysts for Water Oxidation. *Chem. Sci.* **2018**, *9* (10), 2762–2767. https://doi.org/10.1039/c7sc05452a.

(4) Zhang, G.; Jia, Y.; Zhang, C.; Xiong, X.; Sun, K.; Chen, R.; Chen, W.; Kuang, Y.; Zheng, L.; Tang, H.; Liu, W.; Liu, J.; Sun, X.; Lin, W. F.; Dai, H. A General Route via Formamide Condensation to Prepare Atomically Dispersed Metal-Nitrogen-Carbon Electrocatalysts for Energy Technologies. *Energy Environ. Sci.* **2019**, *12* (4), 1317–1325. https://doi.org/10.1039/c9ee00162j.

(5) Joo, J.; Na, H. Bin; Yu, T.; Yu, J. H.; Kim, Y. W.; Wu, F.; Zhang, J. Z.; Hyeon, T. Generalized and Facile Synthesis of Semiconducting Metal Sulfide Nanocrystals. *J. Am. Chem. Soc.* **2003**, *125* (36), 11100–11105. https://doi.org/10.1021/ja0357902.

(6) Ghezelbash, A.; Korgel, B. A. Nickel Sulfide and Copper Sulfide Nanocrystal Synthesis and Polymorphism. *Langmuir* **2005**, *21* (21), 9451–9456. https://doi.org/10.1021/la051196p.

(7) Zhao, L.; Jia, J.; Yang, Z.; Yu, J.; Wang, A.; Sang, Y.; Zhou, W.; Liu, H. One-Step Synthesis of CdS Nanoparticles/MoS_2 Nanosheets Heterostructure on Porous Molybdenum Sheet for Enhanced Photocatalytic H_2 Evolution. *Appl. Catal. B Environ.* **2017**, *210*, 290–296. https://doi.org/10.1016/j.apcatb.2017.04.003.

(8) Huang, K. J.; Zhang, J. Z.; Fan, Y. One-Step Solvothermal Synthesis of Different Morphologies CuS Nanosheets Compared as Supercapacitor Electrode Materials. *J. Alloys Compd.* **2015**, *625*, 158–163. https://doi.org/10.1016/j.jallcom.2014.11.137.

(9) Liu, X. J.; Xu, Z. Z.; Ahn, H. J.; Lyu, S. K.; Ahn, I. S. Electrochemical Characteristics of Cathode Materials NiS_2 and Fe-Doped NiS_2 Synthesized by Mechanical Alloying for Lithium-Ion Batteries. *Powder Technol.* **2012**, *229*, 24–29. https://doi.org/10.1016/j.powtec.2012.05.035.

(10) Chen, Y.; Kanan, M. W. Tin Oxide Dependence of the CO_2 Reduction Efficiency on Tin Electrodes and Enhanced Activity for Tin/Tin Oxide Thin-Film Catalysts. *J. Am. Chem. Soc.* **2012**, *134* (4), 1986–1989. https://doi.org/10.1021/ja2108799.

(11) Qiao, J.; Liu, Y.; Hong, F.; Zhang, J. A Review of Catalysts for the Electroreduction of Carbon Dioxide to Produce Low-Carbon Fuels. *Chem. Soc. Rev.* **2014**, *43* (2), 631–675. https://doi.org/10.1039/c3cs60323g.

(12) Li, F.; Chen, L.; Knowles, G. P.; MacFarlane, D. R.; Zhang, J. Hierarchical Mesoporous SnO_2 Nanosheets on Carbon Cloth: A Robust and Flexible Electrocatalyst for CO_2 Reduction with High Efficiency and Selectivity. *Angew. Chemie - Int. Ed.* **2017**, *56* (2), 505–509. https://doi.org/10.1002/anie.201608279.

(13) Zhao, Z.; Peng, X.; Liu, X.; Sun, X.; Shi, J.; Han, L.; Li, G.; Luo, J. Efficient and Stable Electroreduction of CO_2 to CH_4 on CuS Nanosheet Arrays. *J. Mater. Chem. A* **2017**, *5* (38), 20239–20243. https://doi.org/10.1039/c7ta05507b.